Daylight Imagery of Ocean Surface Waves for Wave Spectra

F. M. MONALDO

The Johns Hopkins University Applied Physics Laboratory, Laurel, MD 20810

R. S. KASEVICH

Raytheon Company, Wayland, MA 01778

(Manuscript received 8 February 1980, in final form 20 October 1980)

ABSTRACT

Both surface-reflected daylight and upwelling light are modeled to second order to help provide a quantitative and physically interpretable description of daylight imagery of ocean surface waves for wave spectra. An image recording of the slope-modulated reflected and upwelled radiance can be optically analyzed to provide the surface slope spectrum as a function of wavenumber for a particular patch on the ocean surface.

Sources of error involved in obtaining ocean spectral information from daylight imagery are outlined and methods of alleviating them discussed. Errors resulting from the nonlinear nature of the transfer function relating wave slope to radiance at the sensor are shown to be minimized using the second-order theory in evaluating potential sensor geometries. The directional sensitivity of daylight imagery to waves traveling in various directions is also evaluated.

A modified Pierson wave spectrum was used to generate numerically a one-dimensional wave-slope profile. This slope profile was used as input to a numerical model that generated a modulation of radiance at the sensor. The spectrum of this radiance modulation agreed favorably with the original Pierson spectrum.

1. Introduction

The modulation of radiance by waves on the sea surface allows for the possibility of inferring the wave structure of the sea surface and to make such inferences without physical contact. Stilwell (1969) proposed an optical method of measuring the two-dimensional wavenumber spectrum using a uniform sky-radiance distribution, a refinement of a technique originally used by Barber (1949). In this method the spectrum of the waves is deduced from the distribution of reflected sea brightness only. Kasevich (1975) extended the theory of the technique by considering first- and second-order variations of sky radiance in elevation. We now further extend the model to include first- and second-order sky-radiance azimuthal variations. In addition, we include upwelling from beneath the surface as well as reflected sky radiance in the model. Heretofore, upwelling has been quantitatively ignored.

The value of a spectral representation is that it can greatly simplify the study of important features of physical processes, i.e., interaction between long and short waves, and phase speed determination. A spectrum, although it constitutes less information than the original data, retains many of the salient features in a form more amenable to interpretation. An ocean surface for which a spectrum can be defined must consist of an unbroken surface with a smooth profile. Precisely, the spectrum is undefined at wind speeds beyond the onset of whitecapping because the surface becomes undefined. Practically, whitecapping diminishes the utility of the spectrum only for wavelengths smaller than the areas disturbed by whitecapping.

The earliest attempt to measure the two-dimensional wavenumber spectrum was undertaken by the Stereo Wave Observation Project (SWOP) (Cote *et al.*, 1960). Stereo photographs of the sea were taken and analyzed presuming a uniform sky-radiance distribution. In the SWOP project, the photographs were taken from two airplanes flying in a precise pattern, while Dobson (1970) used a ship as a platform. From the resulting stereo photographs, the wave heights were determined as a function of position. The data were corrected for various sources of error, and the spatial correlation coefficient and wavenumber spectrum of the surface were determined. In addition to the difficulties of obtaining the stereo pair, the data reduction involved in this technique is generally tedious and slow.

The method of Stilwell and Barber involves a procedure in which a single photograph of the ocean

0022-3670/81/020272-12$07.00

surface is recorded and optically Fourier analyzed. Since the sky radiance reflected from the surface and upwelling radiance transmitted through the surface are a function of local surface slope, the radiance from each point on the surface is modulated as the local slope changes. This radiance modulation is then recorded on film. By choosing the correct camera viewing angles with respect to the sun and the sea surface, and by selecting the proper film characteristics, an image of the sea surface can be obtained such that the relation between surface wave slope and amplitude transmittance of the film is nearly linear. Such linear relationships make it possible to obtain reliable spectral information about the sea surface by optical Fourier analysis. The development of coherent optical processing techniques has made the analysis of photographic negatives a practical method of deducing the spectral properties of waves and their directional characteristics. Optical Fourier analysis of the film-amplitude transmittance performs exactly and very rapidly a mathematical transformation which is otherwise lengthy and somewhat difficult (Goodman, 1968).

It is also possible to image ocean waves using a television camera as a sensor. The Fourier transform of such images can be obtained digitally. Gotwols and Irani (1980) have been able to measure short-gravity-wave phase velocity using television images.

Motivation for the present study of this technique was derived from two programs. First, time series photographs based on the application of this technique were exposed during the Joint North Sea Wave Project (JONSWAP) in 1975 by R. Kasevich and T. Flanagan (Konrad *et al.*, 1976; Konrad and Monaldo, 1979). Second, in an effort to secure short-wave spectral information to evaluate the ability of the synthetic-aperture radar on the Seasat satellite to monitor the ocean surface, time series photographs of the ocean surface were taken during the Duck-X Experiment off North Carolina in 1978 (Monaldo and Beal, 1979). Data derived from these programs are being analyzed using the second-order model and results are described in a forthcoming paper.

In investigating daylight imagery of ocean waves, our efforts were directed at identifying and minimizing potential errors. We will first outline the errors thus far identified and methods of dealing with them. Alleviating some of the errors requires selecting a geometry with an appropriate transfer function relating wave slope to radiance. The model of daylight imagery of ocean waves developed in a subsequent section will allow the experimenter to select an appropriate sensor geometry and to investigate sources of error in this technique.

TABLE 1. Problem areas.

Point source errors
• nonlinear wave slope to radiance transformation
• nonlinear radiance to sensor output transformation
Imaging errors
• variation of wave slope to radiance transformation across the image
• scale distortion
• spatial projection
• spatial filtering

2. Error sources

Obtaining reliable two-dimensional ocean spectra from optical images is based on the assumption that wave slope on the surface can be related to radiance variation at the sensor and ultimately to sensor output (either film transmittance or television electrical output) in such a way that Fourier transforms that meaningfully relate to ocean slope spectra can be performed on this output.

There are several important sources of error associated with the practical application of this technique that should be discussed before the theory is presented. These problem areas can be divided into two categories: point source errors and imaging errors (Monaldo and Chapman, 1979; Chapman and Monaldo, 1979) (Table 1).

a. Point source errors

Point source errors are errors characterizing a point transformation. Consider a particular point on the ocean. The wave slope at that point reflects radiance from a particular part of the sky and transmits radiance from beneath the surface. The radiance from the sky is reduced by the reflection coefficient, the upwelling radiance is reduced by the transmission coefficient, and the sum of the resulting radiances is projected to the sensor. The radiance at the sensor is then converted to sensor output. Nonlinearities in the transfer function relating wave slope to sensor output can cause distortion in the Fourier-transform process.

Point source errors can be divided into two categories: 1) the nonlinearity of the transfer function relating wave slope to incident radiance, and 2) the nonlinearity of the transfer function relating radiance to sensor output, e.g., the curve relating radiance to film-amplitude transmittance.

The model for daylight imagery discussed in this paper provides a way of characterizing the function relating wave slope to radiance so that the linearity of the transfer function can be evaluated for various candidate geometries. In this way geometries that minimize the nonlinearity in the transfer function can be selected.

The nonlinearity introduced by the sensor must be evaluated on a case-by-case basis.

b. Imaging errors

Imaging errors result from the fact that this imaging process is not simply a point transformation but rather the continuous mapping of a wave surface onto a two-dimensional sensor-output profile. This mapping causes a different type of error.

The first type of imaging error is that of the variation of the wave-slope-to-radiance transfer function across the image. It is important to remember that even if the function were perfectly linear, it still would be different on different parts of the image. The effect of this error on the resulting slope spectrum is small if the sensor field of view is limited.

The second type of imaging error is that of scale distortion. Because the sensors make oblique angles with respect to the ocean surface, waves of the same length will appear to have different wavelengths on different parts of the image. Angles on such images are similarly distorted. Scale distortion degrades resolution in wavenumber and angle in the final two-dimensional spectrum. Scale distortion can be dealt with in several ways.

1) Careful sensor geometry selection can minimize the loss in spectral resolution. Sensor depression angles near nadir help to reduce scale distortion.

2) Gaussian or Hanning filtering in the Fourier-transform process can weight the waves in the center of the image, more heavily then the waves at the edges of the image, where scale distortion is the greatest problem.

3) If data are digitally recorded, the scale distortion can be corrected digitally. This correction, however, will tend to be at the expense of spatial resolution.

4) New perspective-control lenses are being currently introduced into 35 mm photography which may be able to reduce further the problems of scale distortion (Goulding, 1976).

The third type of imaging error is that of spatial projection (Saunders, 1967). Because of the oblique angle the sensor axis makes with the sea surface and the finite height of real surface waves, the area of a given facet on the far side of a wave projected on the sensor area is smaller than the projection of a similar facet on the near side of the wave. This will result in a skewing of the radiance distribution at the sensor not present in the actual surface-slope distribution. It is not expected that the skewness of the distribution will distort optically derived slope spectra; however, the magnitude of this effect has yet to be ascertained.

The fourth type of imaging error is the spatial filtering of the ocean-slope spectrum by the optical sensor system. This problem involves the loss of spectral information at short wavelengths arising from inadequate system spatial resolution. The problem can be solved by designing systems with sufficient resolution to detect the smallest wavelength of interest. In any case, the impulse response function of any sensor must be used in correcting spectral data.

Stilwell (1969) considered the effect of waves beyond the resolving ability of the camera imaging system. He concluded that subresolution waves tend to smooth out the sky variations. Their existence "allow the use of photographic procedures on days when the sky is far from a monotonic function . . ." and "may extend the environmental conditions under which optical transforms are useful."

Analysis of the point-source and imaging errors should be treated differently. Point-source errors are more easily evaluated and the use of system models to estimate point-source errors is a good approach in determining the existence of potential errors and selecting potential sensor geometries suitable for the application of this technique. More sophisticated use of system models, however, should be made to estimate system errors introduced by imaging errors.

A possible objection to the use of this technique to obtain two-dimensional spectra has been presented by Peppers and Ostrem (1978). They have properly pointed out that the transfer function between ocean wave slope and radiance incident to the sensor is not unique. A given radiance value could be the result of either of two wave slopes traveling in two different directions. The two-dimensional Fourier-transform process actually resolves this ambiguity, however, by separating wave trains by direction as well as wavenumber. As long as the sea images are recorded with the goal of obtaining slope spectra and not actual surface slopes, the ambiguity suggested by Peppers and Ostrem is not relevant.

3. Model of daylight imagery of ocean waves

A second-order and an exact geometric-optics model have been developed to describe the functional relationship between sea surface slope and reflected and upwelled radiance for three-dimensional surface geometry and two-dimensional sky radiance. Normally one might neglect the second-order model and rely solely on the exact calculation. As we shall see, the second-order model is quantitatively close to the exact calculation, and furthermore the nature of the second-order model allows for the extraction of physical insights more difficult to obtain from the exact model. The first input into these models is the sky-radiance distribu-

tion. It is therefore of benefit to describe the distribution here.

a. Sky-radiance distribution

Pokrowski (1929) has developed an analytic expression based on Rayleigh scattering for the sky-radiance distribution as a function of sun angle for a clear day. The radiance L_s of a point in the sky is given by

$$L_s = L_0 \left(\frac{1 + \cos^2\mu}{1 - \cos\mu} + k \right) \times [1 - \exp(-0.32/\sin\theta_1)], \quad (1)$$

where L_0 is a constant, in units of energy per unit area, k the secondary scattering coefficient, θ_1 the elevation angle of the observed point in the sky, and μ the angle between the sun position and the observed point in the sky. The term $\cos\mu$ can be expressed as $\sin\theta_1 \sin\theta_2 + \cos\theta_1 \cos\theta_2 \cos\alpha$, where θ_2 is the sun elevation angle and α the azimuth difference between the sun and the observed point in the sky. The scattering constant k varies from 0 to 5. The value 0 corresponds to a perfectly clear day, whereas the value 5 corresponds to hazy day with particulates and aerosols as secondary scatterers. The k value can also depend on the electromagnetic frequency range considered. The lower the frequency, the more the secondary scattering. Hopkinson (1954) essentially confirmed this expression by experiments conducted in Stockholm.

A formula has been developed (Walsh, 1960) for expressing the sky-radiance distribution for a uniformly overcast day, i.e.,

$$L_s = L_z(1 + 2\sin\theta_1)/3, \quad (2)$$

where L_z, measured in units of energy per unit area, is the radiance at zenith. There is no azimuth dependence in this expression. Our emphasis in this paper shall be limited to clear days. It is possible, however, to treat uniformly overcast days in manner analogous to that in which clear days are treated in this paper.

The polarization of the sky is another important consideration because it affects the intensity of radiance incident on the sensor. The degree of polarization, i.e., the fraction of radiance that is not randomly polarized, can be expressed as $(1 - \cos^2\mu)/(1 + \cos^2\mu)$ (Humphreys, 1929, p. 551). The direction of polarization can be obtained by noting that the polarization vector is perpendicular to the plane defined by a line joining the observer and the sun and one joining the observer and the observed point in the sky (Wehner, 1976; Walker, 1978). In addition, one-half of the randomly polarized light radiance can be considered as horizontally or vertically polarized. It is then possible to calculate the fraction of radiance that is either horizontally or vertically polarized from any part of the sky. By combining the expressions for polarization and radiance, the distribution of either horizontally or vertically polarized radiance of a clear sky can be expressed analytically.

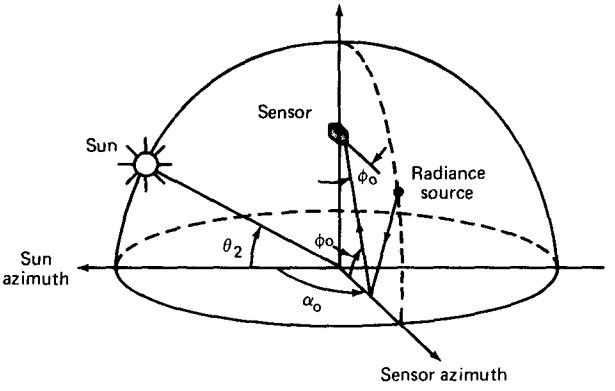

FIG. 1. Sensor geometry with respect to sun and ocean.

b. Second-order model

The second-order model of daylight imagery of ocean waves is essentially a model depicting how wave slopes on the sea surface are mapped into a radiance distribution incident on the sensor.

In developing the model, the sea surface is considered without foam or whitecaps. The only scatterers are waves with two simplifying aspects: 1) the slopes are usually smaller than 30°; hence, multiple reflections and shadowing can be ignored; and 2) the ratios of visible-light wavelength to the radius of curvature and to the wavelength of water waves are both small in comparison with typical wave slopes. Geometric optics can therefore be used with adequate accuracy for study the scattering of visible radiance (Austin, 1974).

In developing the second-order model, we shall consider the distribution of upwelling radiance just beneath the surface and how it is modulated by surface slope. Although upwelling can be represented in our second-order model, an analytic expression for the upwelling radiance distribution does not yet exist. Plass, *et al.* (1976) have used Monte Carlo simulation techniques to calculate numerically the upwelling radiance. Although the results of such calculations are not represented in closed form, it is possible to evaluate our second-order model from the results of Plass *et al.* (1976) for certain important sensor geometries.

The sensor configuration is defined in Fig. 1. The sun is at an angle of elevation θ_2 above the horizon, the sensor is pointed along an azimuth α_0 from the azimuth of the sun, and the optical axis of the sensor

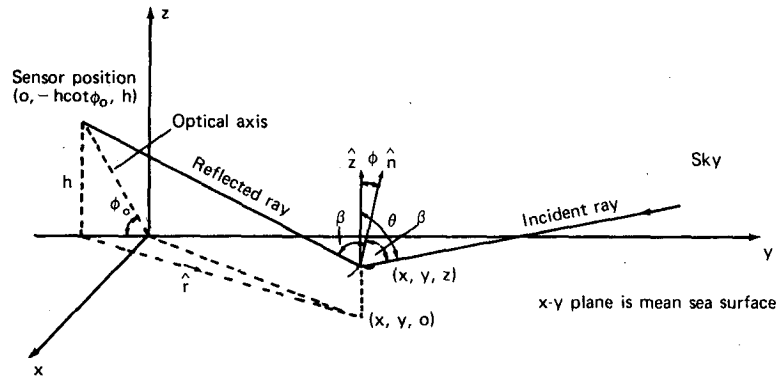

FIG. 2. Detailed geometric configuration.

makes an angle ϕ_0 with the sea surface along the viewing azimuth.

Fig. 2 shows a more detailed picture of our geometry in an (x, y, z) coordinate system. Here h is the sensor height above the mean sea surface and the sensor is located in this coordinate system at $(0, -h \cot \phi_0, h)$. The vector $\hat{\mathbf{z}}$ is the unit vector pointing in the z direction and $\hat{\mathbf{n}}$ is the local unit vector normal to the sea surface. The angle between these two unit vectors is ϕ. The angle β is the angle between either the reflected or incident ray and the local normal. The angle θ is defined as the angle between $\hat{\mathbf{z}}$ and the incident ray. The unit vector pointing from point $(0, -h \cot \phi_0, 0)$ to $(x, y, 0)$ is defined as $\hat{\mathbf{r}}$. The angle between $\hat{\mathbf{r}}$ and the y axis is ξ.

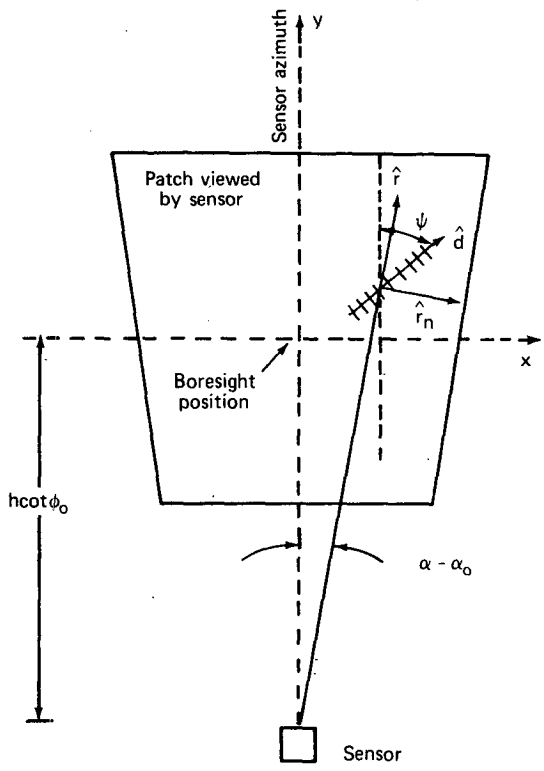

FIG. 3. Ocean-patch geometry with respect to sensor.

We consider a patch on the sea surface that is seen by the sensor (see Fig. 3). Here $\hat{\mathbf{r}}_n$ is defined as the unit vector normal to $\hat{\mathbf{r}}$, and $\hat{\mathbf{d}}$ is the unit vector on the sea surface in the direction of propagation of a wave train. The angle between $\hat{\mathbf{d}}$ and the y axis is ψ. A horizontal polarizer should be placed in front of any sensor imaging the sea, since taking photographs through a horizontal polarizer avoids the double-valued and hence nonlinear nature of the vertical polarization reflectivity curve. The fundamental expression for the radiance incident on the detector $I_s(\phi)$ resulting from only reflected sky radiance is derived from the product of horizontally polarized sky radiance $L_s(\theta_1, \theta_2, \alpha)$ and the Fresnel reflectivity $\Gamma(\beta)$ for horizontal polarization. The angles θ_1 and α prescribe the part of the sky from which the radiance is reflected. For this case, $\theta_1 = 90° - \theta$ and α is the angle between the sun azimuth and a line connecting the origin and the point on the surface in question. So $L_s(\theta_1, \theta_2, \alpha)$ can be written as $L_s(\theta, \theta_2, \alpha)$. $L_s(\theta, \theta_2, \alpha)$ will only include horizontally polarized sky radiance and $\Gamma(\beta)$ will only include reflectivity for horizontally polarized radiance. We will now drop the subscript s on L. When L appears without subscript it is assumed to refer to sky radiance.

$I_s(\phi)$ can be expressed as a second-order Taylor-series expansion of the product of $L(\theta, \theta_2, \alpha)$ and $\Gamma(\beta)$. Specifically, after considerable mathematical manipulation,

$$\begin{aligned} I_s(\phi) = I_s(\phi = 0) &+ \phi G_1(\hat{\mathbf{r}}\cdot\hat{\mathbf{d}}) + \phi G_2 2 \cot\theta_0(\hat{\mathbf{r}}_n\cdot\hat{\mathbf{d}}) \\ &+ \tfrac{1}{2}\phi^2 G_3 \cot\theta_0(\hat{\mathbf{r}}_n\cdot\hat{\mathbf{d}})^2 + \tfrac{1}{2}\phi^2 G_4(\hat{\mathbf{r}}\cdot\hat{\mathbf{d}})^2 \\ &+ \tfrac{1}{2}\phi^2 G_5 4(1 - 2\cot^2\theta_0)(\hat{\mathbf{r}}\cdot\hat{\mathbf{d}})(\hat{\mathbf{r}}_n\cdot\hat{\mathbf{d}}) \\ &+ \tfrac{1}{2}\phi^2 G_6 4 \cot\theta_0(\hat{\mathbf{r}}_n\cdot\hat{\mathbf{d}})^2 \\ &+ \tfrac{1}{2}\phi^2 G_7 2 \cot\theta_0(\hat{\mathbf{r}}\cdot\hat{\mathbf{d}})(\hat{\mathbf{r}}_n\cdot\hat{\mathbf{d}}). \quad (3) \end{aligned}$$

In this expansion θ_0 is the value of θ when $\phi = 0$, and the G factors are constants independent of ϕ, but dependent on θ_0, θ_2, α. If α is the azimuth angle with respect to the sun of the sky-radiance source, and α_0 is the azimuth of the sensor, then

$$I_s(\phi = 0) = L(\theta_0, \alpha_0)\Gamma(\theta_0), \tag{4}$$

$$G_1 = \left\{ L(\theta, \alpha) \frac{d\Gamma(\beta)}{d\beta} + 2\Gamma(\beta) \frac{\partial L(\theta, \alpha)}{\partial \theta} \right\}_{\phi=0}, \tag{5}$$

$$G_2 = \left\{ \Gamma(\beta) \frac{\partial L(\theta, \alpha)}{\partial \alpha} \right\}_{\phi=0}, \tag{6}$$

$$G_3 = \left\{ L(\theta, \alpha) \frac{d\Gamma(\beta)}{d\beta} + 4\Gamma(\beta) \frac{\partial L(\theta, \alpha)}{\partial \theta} \right\}_{\phi=0}, \tag{7}$$

$$G_4 = \left\{ L(\theta, \alpha) \frac{d^w\Gamma(\beta)}{d\beta^2} + 4\Gamma(\beta) \frac{\partial^2 L(\theta, \alpha)}{\partial \alpha^2} + 4 \frac{d\Gamma(\beta)}{d\beta} \frac{\partial L(\theta, \alpha)}{\partial \alpha} \right\}_{\phi=0}, \tag{8}$$

$$G_5 = G_2 = \left\{ \Gamma(\beta) \frac{\partial L(\theta, \alpha)}{\partial \alpha} \right\}_{\phi=0}, \tag{9}$$

$$G_6 = \left\{ \Gamma(\beta) \frac{\partial^2 L(\theta, \alpha)}{\partial \alpha^2} \right\}_{\phi=0}, \tag{10}$$

$$G_7 = \left\{ 2 \frac{\partial L(\theta, \alpha)}{\partial \alpha} \frac{d\Gamma(\beta)}{d\beta} + 4\Gamma(\beta) \frac{\partial^2 L(\theta, \alpha)}{\partial \alpha \partial \theta} \right\}_{\phi=0}. \tag{11}$$

The unit vectors $\hat{\mathbf{r}}$, $\hat{\mathbf{r}}_n$ and $\hat{\mathbf{d}}$ are given by

$$\hat{\mathbf{r}} = \frac{x\hat{\mathbf{x}} + \hat{\mathbf{y}}(y + h \cot\phi_0)}{[x^2 + (y + h \cot\phi_0)^2]^{1/2}} \tag{12}$$

$$= \hat{\mathbf{x}} \sin\xi + \hat{\mathbf{y}} \cos\xi, \tag{13}$$

$$\hat{\mathbf{r}}_n = \hat{\mathbf{x}} \cos\xi - \hat{\mathbf{y}} \sin\xi, \tag{14}$$

$$\hat{\mathbf{d}} = \hat{\mathbf{x}} \sin\psi + \hat{\mathbf{y}} \cos\psi, \tag{15}$$

where ξ equals $\cos^{-1}(\hat{\mathbf{y}} \cdot \hat{\mathbf{r}})$.

The complete function, $I(\phi)$, describing radiance incident to the sensor versus slope is the sum of $I_s(\phi)$, the part due to reflected sky radiance, and $I_u(\phi)$, the contribution due to upwelling radiance from beneath the surface. We now express $I_u(\phi)$ as a second-order expansion.

The geometry used in considering upwelling is shown in Fig. 4. The unit vector defining the direction from the surface to the sensor can be related to the unit vector describing the direction of the upwelling radiance ray by Snell's law. Specifically, $B = \sin^{-1}(\sin\beta/1.34)$, where B is measured from the local normal. In turn, B and the surface-

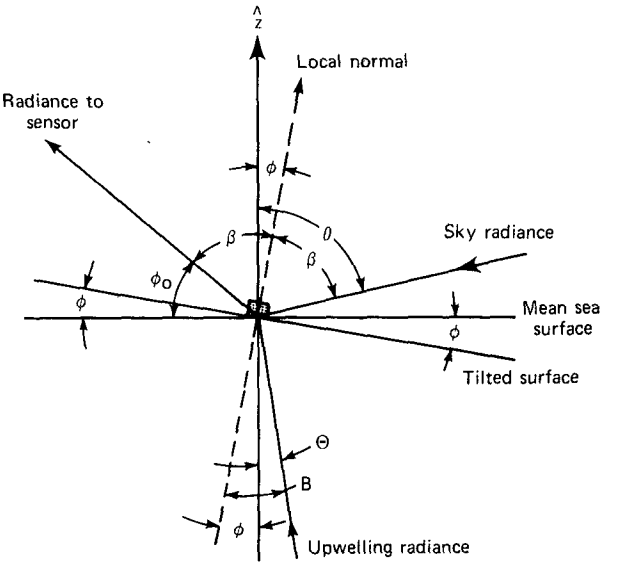

FIG. 4. Geometry specifying origins of both sky and upwelling radiances.

wave slope define two new angles Θ and A. The angle Θ is measured from the negative z axis to the upwelling radiance ray. The angle between the y axis and the projection of the upwelling radiance ray onto the (x, y) plane is defined as A.

Formally, the distribution of upwelling radiance can be given by $L_u(\Theta, A)$. Merely stating the parameters on which $L_u(\Theta, A)$ depends does not allow us to express such dependences analytically. As mentioned earlier, the upwelling distribution can only be determined numerically.

The Monte Carlo calculations of Plass *et al.* (1976) indicate that, although for certain sensor geometries pointing near nadir ($\phi_0 = 90°$), upwelling light may be the dominant radiance source, upwelling just before reaching the air-sea interface is "largely independent of angle of observation." The amount of radiance due to reflection of sky radiance varies tremendously as a function of angle. At viewing angles close to the horizontal, surface-reflected sky radiance is the dominant radiance source.

In order to expand $I_u(\phi)$ to second order, we make the realistic assumption that $L_u(\Theta, A)$ is constant so that modulation of upwelling radiance is solely the effect of modulation of the transmittance coefficient due to variations in local surface slope. Specifically, partial derivatives with respect to Θ and A are equal to zero. The magnitude of the upwelling constant is defined by the parameter R. This parameter equals the ratio of reflected sky radiance to upwelling radiance-transmitted through the surface at nadir. Typical values of R allow for the numerical evaluation of $I_u(\phi)$ expanded to second order.

$I_u(\phi)$ can be expressed by

$$I_u(\phi) = I_u(\phi = 0) + \phi H_1 \cos\beta_0(1.34\cos B_0)^{-1}(\hat{\mathbf{r}}\cdot\hat{\mathbf{d}}) + \tfrac{1}{2}\phi^2 H_1[\cos^2\beta_0 \tan B_0(1.34\cos B_0)^{-2} - \sin\beta_0(1.34\cos B_0)^{-1}](\hat{\mathbf{r}}\cdot\hat{\mathbf{d}})^2 + \tfrac{1}{2}\phi^2 H_1 \cos\beta_0 \cot\theta_0(1.34\cos B_0)^{-2}(\hat{\mathbf{r}}_n\cdot\hat{\mathbf{d}})^2 + \tfrac{1}{2}\phi^2 H_2 \cos^2\beta_0(1.34\cos B_0)^{-2}(\hat{\mathbf{r}}\cdot\hat{\mathbf{d}})^2. \quad (16)$$

The quantities β_0 and B_0 are the values of β and B when $\phi = 0$. The constants $I_u(\phi = 0)$, H_1 and H_2 are given by

$$I_u(\phi = 0) = [L_u(\Theta, A)\Upsilon(B)]_{\phi=0}, \quad (17)$$

$$H_1 = \left[L_u(\Theta, A)\,\frac{d\Upsilon(B)}{dB}\right]_{\phi=0}, \quad (18)$$

$$H_2 = \left[L_u(\Theta, A)\,\frac{d^2\Upsilon(B)}{dB^2}\right]_{\phi=0}. \quad (19)$$

For reasons mentioned earlier the sensor is designed to be responsive only to horizontally polarized radiance. Therefore $L_u(\Theta, A)$ will only include horizontally polarized upwelling radiance and $\Upsilon(B)$ is the transmission coefficient for horizontally polarized radiance.

The sum $I_s(\phi) + I_u(\phi)$ now gives a second-order expansion of the radiance incident on the sensor as a function of wave slope.

The following special cases involving only first-order results are evaluated to assist in the physical interpretation of the model.

Consider the first-order results with no azimuthal sky-radiance dependence $[\partial L(\theta, \alpha)/\partial\alpha = 0]$, which would be the case with an overcast sky. Then the expression for $I(\phi)$ becomes

$$I(\phi) = I_s(\phi = 0) + I_u(\phi = 0) + \phi[G_1 + H_1 \cos\beta_0(1.34\cos B_0)^{-1}](\hat{\mathbf{r}}\cdot\hat{\mathbf{d}}). \quad (20)$$

The slope modulation term in (20) indicates that $I(\phi)$, for this case, is sensitive to the direction of wave propagation ($\hat{\mathbf{d}}$) with respect to the azimuth direction of the reflecting point ($\hat{\mathbf{r}}$). Maximum slope modulation occurs for waves propagating in the $\hat{\mathbf{r}}$ direction, and slope modulation is nonexistent in the $\hat{\mathbf{r}}_n$ direction. For a slope angle ϕ such that the small-angle approximation can be used, $I(\phi)$ may be expressed as

$$I(\phi) = I_s(\phi = 0) + I_u(\phi = 0) + \left(\frac{\partial\eta}{\partial x}\sin\xi + \frac{\partial\eta}{\partial y}\cos\xi\right) \times [G_1 + H_1 \cos\beta_0(1.34\cos B_0)^{-1}], \quad (21)$$

$$= I_s(\phi = 0) + I_u(\phi = 0) + |\nabla\eta| \cos(\psi - \xi) \times [G_1 + H_1 \cos\beta_0(1.34\cos B_0)^{-1}], \quad (22)$$

where η is the waveheight and $|\nabla\eta|$ is the magnitude of the gradient of the waveheight of point (x, y) within the detector field of view. The vector wave slope is

$$\mathbf{S} = \nabla\eta = \hat{\mathbf{x}}\frac{\partial\eta}{\partial x} + \hat{\mathbf{y}}\frac{\partial\eta}{\partial y} \quad \text{and} \quad \phi\hat{\mathbf{d}} = \mathbf{S}. \quad (23)$$

For $\hat{\mathbf{r}}$ aligned along the sensor azimuth direction ($\xi = 0°$) and a wave propagating at the azimuth angle $\psi = 0°$, only the slope component $\partial\eta/\partial y$ will result in modulation of $I(\phi)$ and for $\psi = 90°$ only the component $\partial\eta/\partial x$ will result in modulation of $I(\phi)$.

We now consider the first-order result with azimuthal light dependence. The expression for $I(\phi)$ becomes

$$I(\phi) = I_s(\phi = 0) + I_u(\phi = 0) + \phi[G_1 + H_1 \cos\beta_0(1.34\cos B_0)^{-1}](\hat{\mathbf{r}}\cdot\hat{\mathbf{d}}) + \phi 2G_2 \cot\theta_0(\hat{\mathbf{r}}_n\cdot\hat{\mathbf{d}}). \quad (24)$$

The additional azimuthal modulation term is

$$\phi 2G_2 \cot\theta_0(\hat{\mathbf{r}}_n\cdot\hat{\mathbf{d}}) = -2G_2 \cot\theta_0\left(\frac{\partial\eta}{\partial x}\cos\xi - \frac{\partial\eta}{\partial y}\sin\xi\right), \quad (25)$$

$$= 2G_2 \cot\theta_0|\nabla\eta| \sin(\psi - \xi). \quad (26)$$

With azimuthal sky-radiance dependence, additional first-order modulation of $I(\phi)$ occurs and this modulation is most sensitive to waves propagating in the $\hat{\mathbf{r}}_n$ direction or across boresite. For $\hat{\mathbf{r}}$ aligned along the sensor azimuth ($\xi = 0°$) the slope-modulated light is

$$I(\phi) = I_s(\phi = 0) + I_u(\phi = 0) - [G_1 + H_1 \cos\beta_0(1.34\cos B_0)^{-1}] \times \frac{\partial\eta}{\partial y} - 2G_2 \cot\theta_0 \frac{\partial\eta}{\partial x}. \quad (27)$$

For sensor viewing angle such that $\cot\theta_0$ is small (small sensor depression angle), the azimuthal modulation is negligible in comparison with the zenith-angle-dependent modulation, $I(\phi) \approx I_s(\phi = 0) + I_u(\phi = 0) + \phi[G_1 + H_1 \cos\beta_0(1.34\cos B_0)^{-1}]\hat{\mathbf{r}}\cdot\hat{\mathbf{d}}$. Even for depression angles as great at 45° where $\cot\theta_0$ is not small and for $\alpha_0 > 90°$, the cosine nature of the $I(\phi)$ as a function of $\psi - \xi$ is retained. The maximum value of $I(\phi)$ will not in general be where $\hat{\mathbf{r}}$ and $\hat{\mathbf{d}}$ are parallel, but where they are separated by a few degrees. Fig. 5 shows how the peak response of radiance to wave-slope variations is slightly shifted by the presence of azimuthal sky-radiance dependence. It is interesting to note that the human eye response to daylight reflected from water waves provides a physical realization of the above light-reflection properties. It is well known,

and can be easily verified, that surface waves can be seen better by looking at wave crests at right angles than by observing them in a direction parallel to themselves. For example, in order to see how the wind makes water ripple on a canal, as a rule, one must look along the direction parallel to the canal. The large cross waves behind a ship can be observed from the bridge while they are practically invisible from the bank (Minnaert, 1954, p. 26).

c. Exact model

Since the Fresnel reflectivity transmittance and sky radiance are known analytically, and we assume that upwelling beneath the surface is a constant, as suggested by Plass *et al.* (1976), it is possible to calculate the function $I(\phi)$ exactly. Such an expression for wave slopes traveling along the sensor azimuth is

$$I(\phi) = I^0\left\{\frac{\cos^2(\phi_0+\phi+\delta)}{\cos^2(\phi_0+\phi-\delta)}\right\}\left\{\left[\frac{1+\cos^2\mu}{1-\cos\mu}\right]\left[1-\exp\left(\frac{-0.32}{\sin\theta_1}\right)\right]\right\}$$
$$\times\left\{\frac{1}{2}(1-D)+\frac{D(\sin\theta_2\cos\theta_1-\sin\theta_1\cos\theta_2\cos\alpha_0)^2}{\sin^2\theta_2\cos^2\theta_1+\cos^2\theta_2\sin^2\theta_1+2\cos\theta_2\sin\theta_2\cos\theta_1\sin\theta_1\cos\alpha_0+\cos^2\theta_2\cos^2\theta_1\sin^2\alpha_0}\right\}$$
$$+ I^1\left\{1-\frac{\cos^2(\phi_0+\phi+\delta)}{\cos^2(\phi_0+\phi-\delta)}\right\}, \quad (28)$$

where I^0 and I^1 are constants making the units of the above expression energy per unit area, $\theta_1 = \phi_0 - 2\phi$, $\delta = \sin^{-1}[\cos(\phi_0+\phi)/1.34]$, $D = (1-\cos^2\mu)/(1+\cos^2\mu)$, and all other angles have the same definitions as before. In this expression the first quantity in braces represents the horizontally polarized Fresnel reflectivity, the second the sky radiance, the third the fraction of sky radiance that is horizontally polarized, and the fourth the horizontally polarized transmittance coefficient. It is straightforward to expand this expression to include wave slopes propagating in various directions.

This exact solution is useful in evaluating the accuracy of the second-order model and in performing numerical modeling. It is difficult, however, to glean physical insight from (28) in the same way that the second-order model allowed for intuitive understanding of the imaging process.

For a typical geometry, and the case where the upwelling contribution is small, the exact model, the second-order model, and the linear approximation for $I(\phi)$ are plotted in Fig. 6. Note that over a fairly broad region around $\phi = 0$, the result from the second-order model is virtually identical to that from the exact model. This conclusion is valid for a broad range of sensor geometries greater than 90° in azimuth from the sun, where the sky-radiance distribution is slowly varying.

Since the second-order expansion is close to the exact solution, the terms of order higher than second can legitimately be ignored in describing the physical processes of this imaging system.

4. Optimization of sensor geometry

Estimates of nonlinearity in the wave-slope-to-radiance transformation in a point-source sense can be made using the second-order model. In order to make the transformation linear, all the terms proportional to ϕ should be made much larger than the terms proportional to ϕ squared.

Consider the second-order expansion for wave slopes propagating along the sensor azimuth. In this case $\hat{\mathbf{r}}_n\cdot\hat{\mathbf{d}} = 0$, $\hat{\mathbf{r}}\cdot\hat{\mathbf{d}} = 1$, and the only terms left in the expansion are

$$I(\phi) = I_s(\phi=0) + I_u(\phi=0) + \phi[G_1 + H_1\cos\beta_0(1.34\cos B_0)^{-1}] + \tfrac{1}{2}\phi^2[H_1\cos^2\beta_0\tan B_0(1.34\cos B_0)^{-2} - H_1\sin\beta_0(1.34\cos B_0)^{-1} + H_2\cos^2\beta_0(1.34\cos B_0)^{-2} + G_4] \quad (29)$$

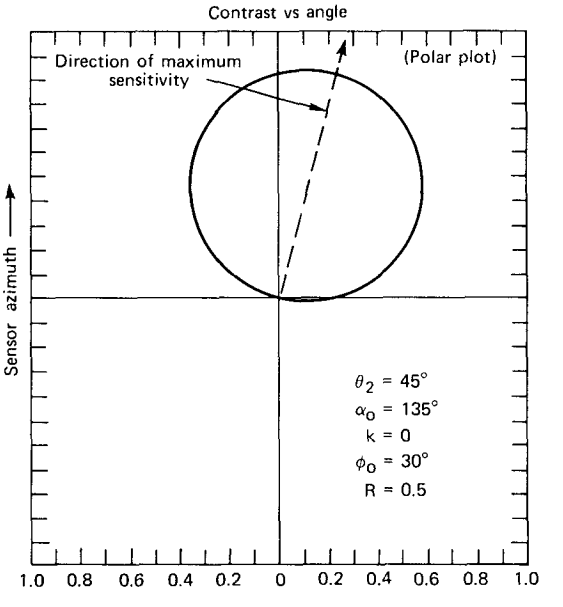

FIG. 5. Magnitude of radiance modulation for wave trains propagating in any direction on the sea surface.

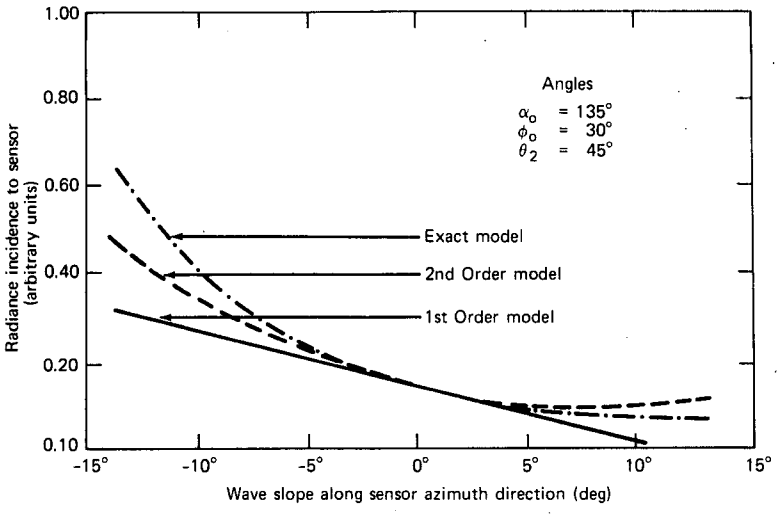

FIG. 6. Comparison of first-order, second-order and exact models of the wave-slope-to-radiance transformation.

or

$$I(\phi) = I_0 + \phi I_1 + \tfrac{1}{2}\phi^2 I_2, \qquad (30)$$

where I_0, I_1 and I_2 can be associated with their bracketed counterparts in (29).

The point transformation of wave slope to radiance can be considered linear when $\phi/2 \ll |I_1/I_2|$. By numerically evaluating $|I_1/I_2|$ for particular sun elevation and azimuth angles, the optimum sensor depression angle to achieve linear response, and thus more accurately record slope spectra, is determined.

Fig. 7 shows $|I_1/I_2|$ versus depression angle, ϕ_0 for a sensor azimuth off the sun of 135°, and a sun elevation angle of 45°. Since the ratio $|I_1/I_2|$ is a direct measure of linearity, the larger the value $|I_1/I_2|$ the more linear the wave-slope-to-radiance transfer function.

The solid line in Fig. 7 depicts the variation in $|I_1/I_2|$ if no upwelling radiance is present, i.e., $R = \infty$. Of interest is the observation that $|I_1/I_2|$ has a sharp minimum at $\phi_0 = 63°$. At that sensor depression angle, the wave-slope-to-radiance transfer function is most nonlinear. An experimenter should thus avoid that sensor geometry that uses $\phi_0 = 63°$.

The dashed line in Fig. 7 depicts the variation in $|I_1/I_2|$ for a realistic value of $R = 0.5$. Specifically, the radiance recorded at the sensor pointed at nadir

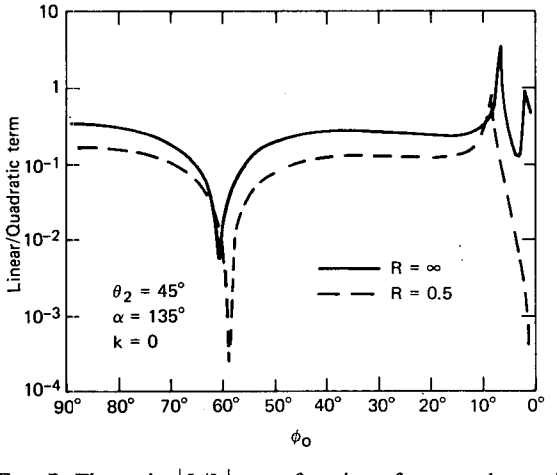

FIG. 7. The ratio $|I_1/I_2|$ as a function of sensor depression angle. The solid line represents the case where the upwelling contribution is ignored and the dashed line the case with a realistic level of upwelling.

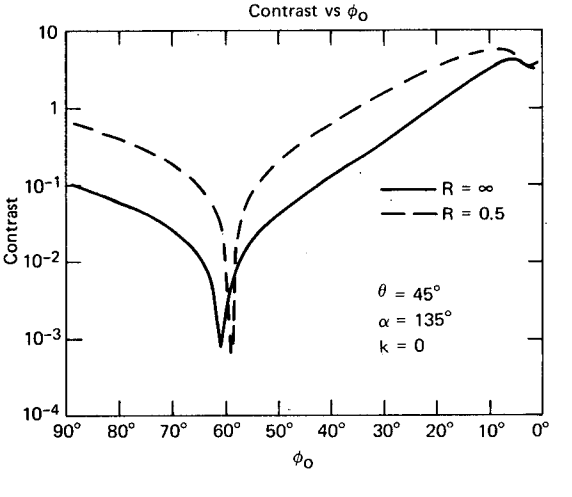

FIG. 8. Contrast as a function of sensor depression angle. The solid line represents the case where the upwelling contribution is ignored and the dashed line the case with a realistic level of upwelling.

($\phi_0 = 90°$) has twice as much transmitted upwelling radiance as reflected sky radiance. For this curve the maximum nonlinearity occurs at $\phi_0 = 59°$.

The curves shown in Fig. 7 are representative of a broad range of sensor geometries for $\theta_2 < 50°$ and $\alpha_0 > 90°$. From these curves two conclusions can be drawn concerning linearity optimization.

First, the addition of realistic levels of upwelling to the second-order method does not appear to alter appreciably those geometries for which linearity is optimized. The general effect of upwelling is to shift the linearity minimum slightly toward smaller values of ϕ_0.

The second is that the linearity ($|I_1/I_2|$) of the wave-slope-to-radiance transformation at any given depression angle is lower with the addition of upwelling. To the extent that radiance wavelength filters and polarization techniques can reduce the contribution of upwelling radiance, they should be employed. The reduction of upwelling radiance will increase the linearity of the transformation between wave slope and radiance.

Not only is it important to provide for maximum linearity, it is also important to determine those sensor geometries which yield the highest contrast, i.e., the highest signal-to-noise ratio. Contrast can be defined as the ratio of the terms linear in ϕ over the average radiance level, i.e.,

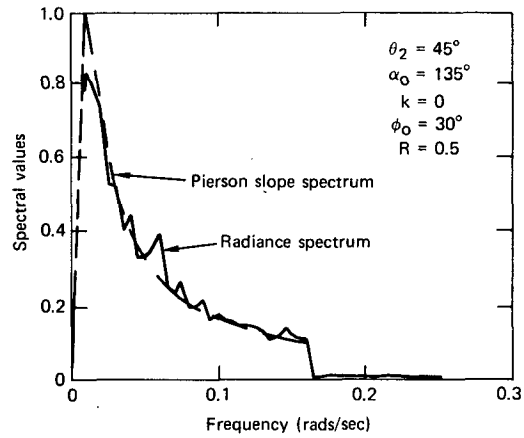

FIG. 9. Comparison of original Pierson spectrum with the ensemble average of 20 radiance spectra. For this geometry, the $|I_1/I_2|$ value indicates that the wave-slope-to-radiance transformation is linear.

$$\text{Contrast} = \frac{G_1(\hat{\mathbf{r}}\cdot\hat{\mathbf{d}}) + 2G_2\cot\theta_0(\hat{\mathbf{r}}_n\cdot\hat{\mathbf{d}}) + H_1\cos\beta(1.34\cos B)^{-1}(\hat{\mathbf{r}}\cdot\hat{\mathbf{d}})}{I_s(\phi = 0) + I_u(\phi = 0)}. \tag{31}$$

Consider how contrast varies as a function of depression angle ϕ_0 when the wave train is parallel to $\hat{\mathbf{r}}$. For this case $\hat{\mathbf{r}}\cdot\hat{\mathbf{d}} = 1$ and $\hat{\mathbf{r}}_n\cdot\hat{\mathbf{d}} = 0$. The solid line in Fig. 8 shows how contrast varies without upwelling present, while the dashed line shows the same for a realistic level of upwelling ($R = 0.5$). Note here that as in the plot showing variations in linearity, the depression angles near $\phi_0 = 60°$ show a minimum of contrast.

The linearity curves in Fig. 7 showed that there were definite depression angles to be avoided. Fig. 8 curves show that one wants depression angles less than 60° to maintain the highest contrast. The scale distortion accompanying very small depression angles, however, suggests that depression angles on the order of 30° are a fair compromise.

5. Numerical modeling

The second-order theory has thus far provided a basis for the optimization of sensor geometries. Once potential geometries have been selected, a more complete investigation of a particular geometry can be performed by numerical simulation.

Numerical simulations have been performed in one dimension (Chapman and Monaldo, 1979). A modified Pierson windwave spectrum (Bjerkaas and Reidel, 1979) is assumed to exist on the surface. A randomly selected phase is associated with each amplitude in the spectrum. The resultant spectrum is inverse-Fourier-transformed to generate a one-dimensional wave-slope profile. This profile is then transformed to a one-dimensional radiance distribution incident on the sensor by means of the exact solution. The transformation used in the simulation excludes the effects of scale distortion and spatial projection.

The radiance variation is then Fourier-transformed. The spectrum so produced is compared to the original spectrum. Any differences are presumed to be caused by irregularities in the transformation of wave slope to radiance.

Fig. 9 shows the original Pierson spectrum for a frictional wind velocity U^* equal to 12 cm s^{-1}, and an ensemble average of 20 radiance spectra. Note that for this particular geometry the two spectra agree closely.

Fig. 10 shows results for a different sensor geometry. For this geometry, the spectra do not closely agree. Because of the nonlinearity of the transfer function, energy is thrown into the higher frequencies, and the measured spectral energy is reduced.

For appropriate geometries, then, the imaging

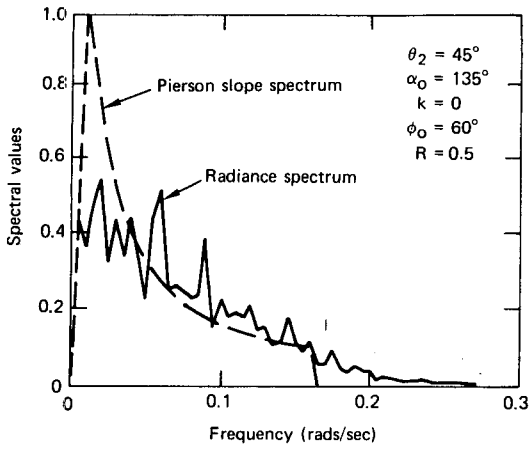

FIG. 10. As in Fig. 9 except that the $|I_1/I_2|$ value indicates that the wave-slope-to-radiance transformation is nonlinear.

process can accurately record wave-slope spectra for waves traveling along the sensor azimuth. Spectra for waves traveling in other directions can be accurately obtained, but it is not yet clear how these other one-dimensional spectra can be quantitatively compared to form a reliable two-dimensional spectrum. Further efforts are being made at the Applied Physics Laboratory of The Johns Hopkins University to extend the numerical simulations to two-dimensional wave-slope profiles.

6. Conclusions

A simple second-order model has been developed to describe the transformation between surface wave slope and radiance incident on an optical sensor. This model includes azimuth as well as elevation variations in the sky-radiance distribution and their effects on the imaging of wave slopes approaching the sensor azimuth from various directions. For the first time such a model also includes upwelling radiance. Comparison between the exact transformation from wave slope to radiance and the second-order model suggests that they yield quantitatively similar results.

Use of the second-order model lent itself to physical interpretations of how wave slopes are imaged. It also indicated a straightforward way of optimizing the linearity and contrast of the transfer function relating wave slope to radiance for various candidate sensor geometries, thereby minimizing sources of error. Upwelling in realistic amounts has not been found to affect significantly sensor-geometry optimization, but to reduce overall linearity.

Simple one-dimensional numerical simulations of the imaging of an analytically generated wave-slope profile demonstrate the utility of this technique in obtaining slope spectra, at least for waves traveling along the sensor's azimuth. A forthcoming paper will use the second-order model and results to analyze measurements of the short-wave modulation by long waves.

Acknowledgments. We should like to acknowledge gratefully the support, encouragement and scientific input of R. C. Beal, R. D. Chapman, K. Hasselmann, I. Katz, T. G. Konrad, D. Ross and J. R. Rowland. The work described in this paper was jointly supported by the National Science Foundation under Grant OCE-7719039, the National Oceanic and Atmospheric Administration and the National Aeronautics and Space Administration under Contract MO-A01-78-00-4330, the Office of Naval Research under Contract N00024-78-C-5384, and the National Oceanic and Atmospheric Administration under Contract 03-6-022-35114.

REFERENCES

Austin, R. W., 1974: The remote sensing of spectral radiance from below the ocean surface. *Optical Aspects of Oceanography*, N. G. Jerlov and E. Steemann-Nielson, Eds., Academic Press, 317–344.

Barber, N. F., 1949: A diffraction analysis of a photograph of the sea. *Nature*, **164**, 485.

Bjerkaas, A. W., and F. W. Reidel, 1979: Proposed model for the elevation spectrum of a wind roughened sea surface. APL/JHU TG-1328, Johns Hopkins University/Applied Physics Laboratory, Laurel, MD, 25 pp. [NTIS ADA083426.]

Chapman, R. D., and F. M. Monaldo, 1979: Non-linear analysis of optical sea surface imagery, imaging errors. *Trans. Amer. Geophys. Union*, **60**, 24.

Cote, L. J., J. O. David, W. Marks, R. J. McGough, E. Mehr, W. J. Pierson, Jr., J. F. Roper, G. Stephenson and R. C. Vetter, 1960: The directional spectrum of a wind generated sea as determined from data obtained by the stereo wave observation project. *Meteor. Pap.*, NYU College of Engineering, **2**, No. 6, 88 pp.

Dobson, E. B., 1970: Measurement of fine scale structure of the sea. *J. Geophys. Res.*, **75**, 2853–2856.

Goodman, J. W., 1968: *Introduction to Fourier Optics*. McGraw-Hill, 287 pp.

Gotwols, B. L. and G. B. Irani, 1980: Optical determination of the phase velocity of short gravity waves. *J. Geophys. Res.*, **85**, 3964–3970.

Goulding, R. D., 1976: 35 mm in architectural photography. *Photomethods*, **19**, 19–21.

Hopkinson, R. G., 1954: Measurement of sky luminance distribution at Stockholm. *J. Opt. Soc. Amer.*, **44**, 455–459.

Humphreys, J., 1929: *Physics of the Air*. McGraw-Hill, 654 pp.

Kasevich, R. S., 1975: Directional wave spectra from daylight scattering. *J. Geophys. Res.*, **80**, 4535–4541.

Konrad, T. G., and F. M. Monaldo, 1979: Fine time scale series of sea surface spectra at selected wavelengths taken from JONSWAP sea photographs. U.S. National Committee, International Union of Radio Science, Programs and Abstracts, National Radio Science Meeting (November), Boulder, CO, 105 pp.*

* Copies available from USNC/URSI, National Academy of Sciences, 2101 Constitution Ave., NW, Washington, DC 20418.

——, R. S. Kasevich, J. R. Rowland and T. W. Flanagan, 1976: Fine time scale, two-dimensional sea surface spectra in the high-frequency range from sea photographs. U.S. National Committee, International Union of Radio Science, Program and Abstracts, 1976 Annual Meeting, Amherst, MA, 103 pp.*

Minnaert, M., 1954: *The Nature of Light and Color in the Open Air*. Dover, 362 pp.

Monaldo, F. M., and R. C. Beal, 1979: Measurements of the 3 to 30 cm slope spectrum from the CERC pier via Stilwell techniques. U.S. National Committee, International Union of Radio Science, Programs and Abstracts, National Radio Science Meeting (November), Boulder, Colorado, 149 pp.*

——, and R. D. Chapman, 1979: Non-linear analysis of optical sea surface imagery, point source errors. *Trans. Amer. Geophys. Union*, **60**, 24.

Peppers, N. A., and J. S. Ostrem, 1978: Determination of wave slopes from photographs of the ocean surface: A new approach. *Appl. Opt.*, **17**, 3450–3458.

Plass, G. N., G. W. Kattawar and J. A. Quinn, 1976: Radiance distribution over a ruffled sea: Contributions from glitter, sky and ocean. *Appl. Opt.*, **15**, 3161–3165.

Pokrowski, G. I., 1929: Distribution of brightness in the sky, *Phys. Z.*, **30**, 697–700.

Saunders, P. M., 1967: Shadowing of the ocean and the existence of the horizon. *J. Geophys. Res.*, **72**, 4643–4649.

Stilwell, Jr., D., 1969: Directional energy spectra of the sea from photographs. *J. Geophys. Res.*, **74**, 1974–1986.

Walker, J., 1978: More about polarizers and how to use them, particularly for studying polarized sunlight. *Sci. Amer.*, **238**, 132–136.

Walsh, J. G. T., 1960: Daylight illumination and sky luminance. *Science of Daylight*, MacDonald Press, 29–58.

Wehner, R., 1976: Polarized light navigation by insects. *Sci. Amer.*, **235**, 106–115.